Supplementary information

A bioinspried tactile scanner for computer haptics

Huimin Li[1], Jianle Lin[1], Shuxin Lin[1], Bowei Jiang[1], Xinghui Liu[2], Weisheng Wu[1], Weiwei Li[3], Emad Iranmanesh[1], Zhongyi Zhou[2], Wenjun Li[4], Kai Wang[1*]

[1]Guangdong Province Key Laboratory of Display Material and Technology, State Key Laboratory of Optoelectronic Materials and Technologies, School of Electronics and Information Technology (School of Microelectronics), Sun Yat-sen University, Guangzhou, Guangdong, China.

[2]Shenzhen Chipwey InnovationTechnologies Co. Ltd., Shenzhen, Guangdong, China.

[3]State Key Laboratory of Microelectronic Devices & Integrated Technology, Institute of Microelectronics, Chinese Academy of Sciences, Beijing, China.

[4]School of Computer Science and Engineering, Sun Yat-sen University, Guangzhou, Guangdong, China.

[*]Corresponding author. E-mail: wangkai23@mail.sysu.edu.cn (K.W.).

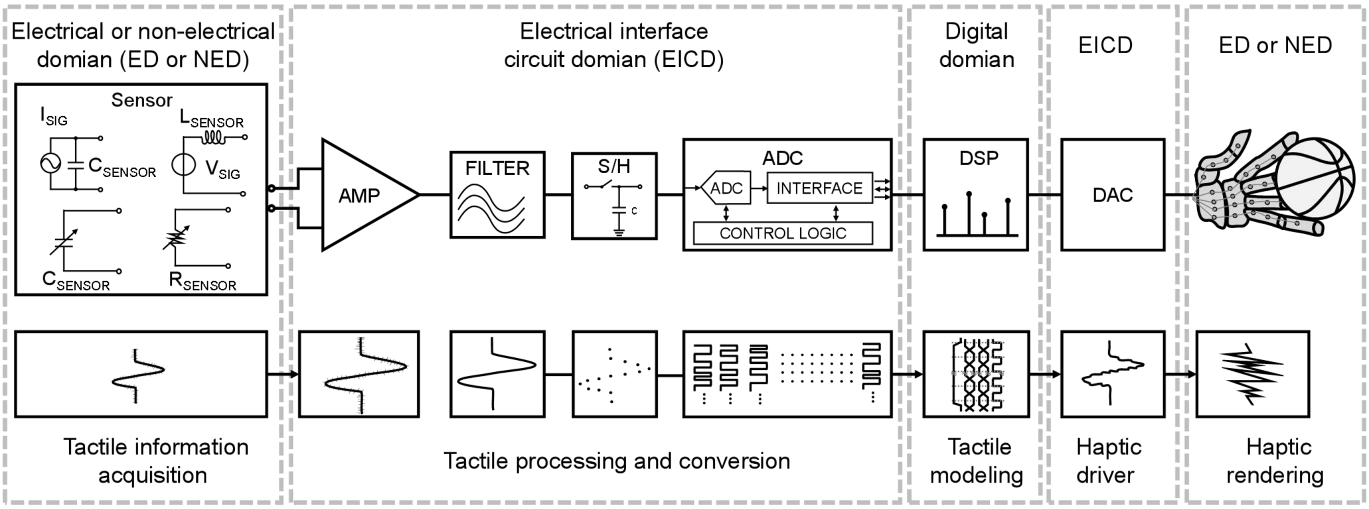

Supplementary Fig. 1. A generic block diagram of a conventional tactile/haptic system. The system consists of electrical or non-electrical domain (ED or NED), electrical interface circuit domain (EICD), and digital domain. Tactile sensory signals are acquired by electrical or non-electrical sensors. The electrical interface circuit processes and converts analog tactile stimuli to digital signals by an analog-to-digital converter (ADC) and further being processed by a digital signal processor (DSP) to generate a tactile sensory model for haptic rendering. A digital-to-analog converter (DAC) is then used to convert the tactile model to an analog driving signal as a haptic rendering signal for redisplaying and recreating the tactile sensation.

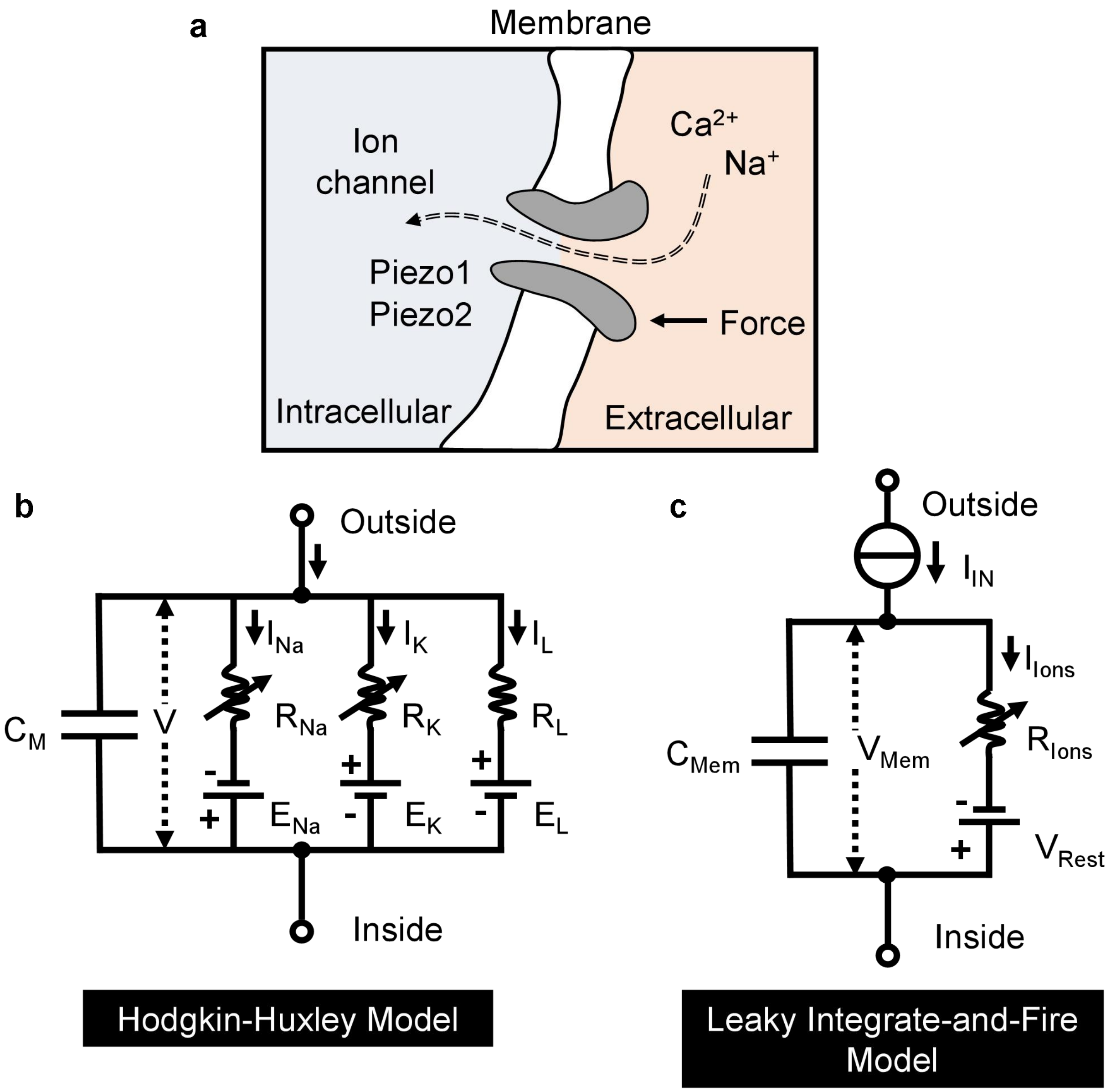

Supplementary Fig. 2. a, Schematic diagram of a neuron cell covered by a cell membrane. The tactile force stimulus induces opening of ion channel, followed by the influx of neurotransmitters (Na^+, Ca^{2+}) into the neuron cell. **b,** Hodgkin-Huxley model from squid axon. **c,** Leaky Integrate-and-Fire model of a neuron.

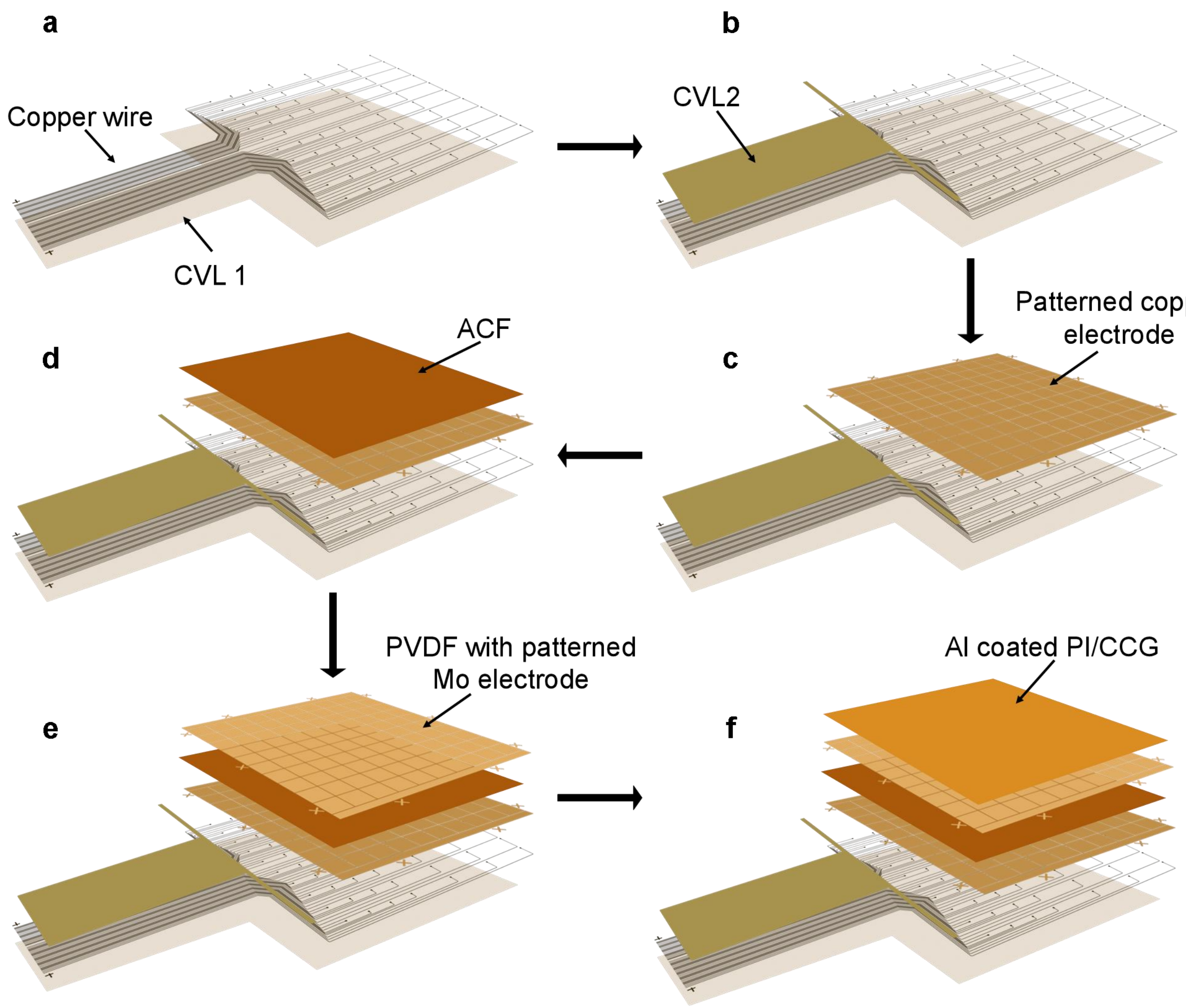

Supplementary Fig. 3. Schematic illustration of steps for making artificial axon sensor array. **a**, Formation of the Cover Layer 1 (CVL1) with copper wiring. **b**, Fabrication of the Cover Layer 2 (CVL2). **c**, Pixel electrode patterning. **d**, Lamination of the anisotropic conductive film (ACF). **e**, Lamination of the polyvinylidene fluoride (PVDF) with molybdenum (Mo) electrode array. **f**, Assembly of the aluminum (Al)-coated polyimide (PI) film and PVDF film with carbon conductive glue (CCG).

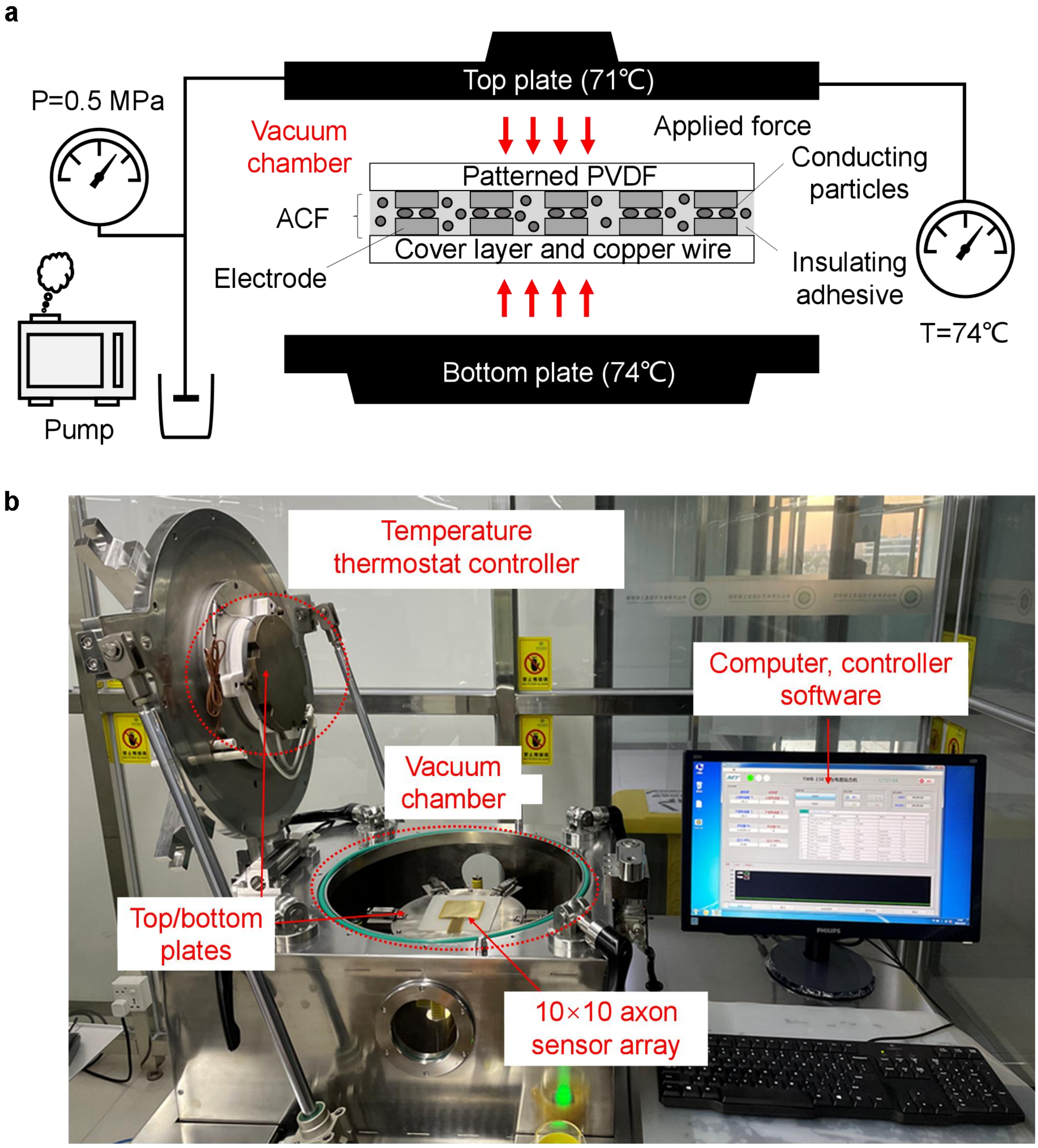

Supplementary Fig. 4. Lamination tool of the artificial axon sensor array. a, Device integration of ACF film and PVDF film with patterned Mo electrode under low temperature (<75 °C) and high pressure (0.5 MPa). **b,** The axon sensor array was placed in chamber environment (TWB-150, Guangzhou KeFu Instrument Co., Guangzhou, China), and various combinations of lamination process were applied in order to attain a successful lamination (Supplementary Table 2).

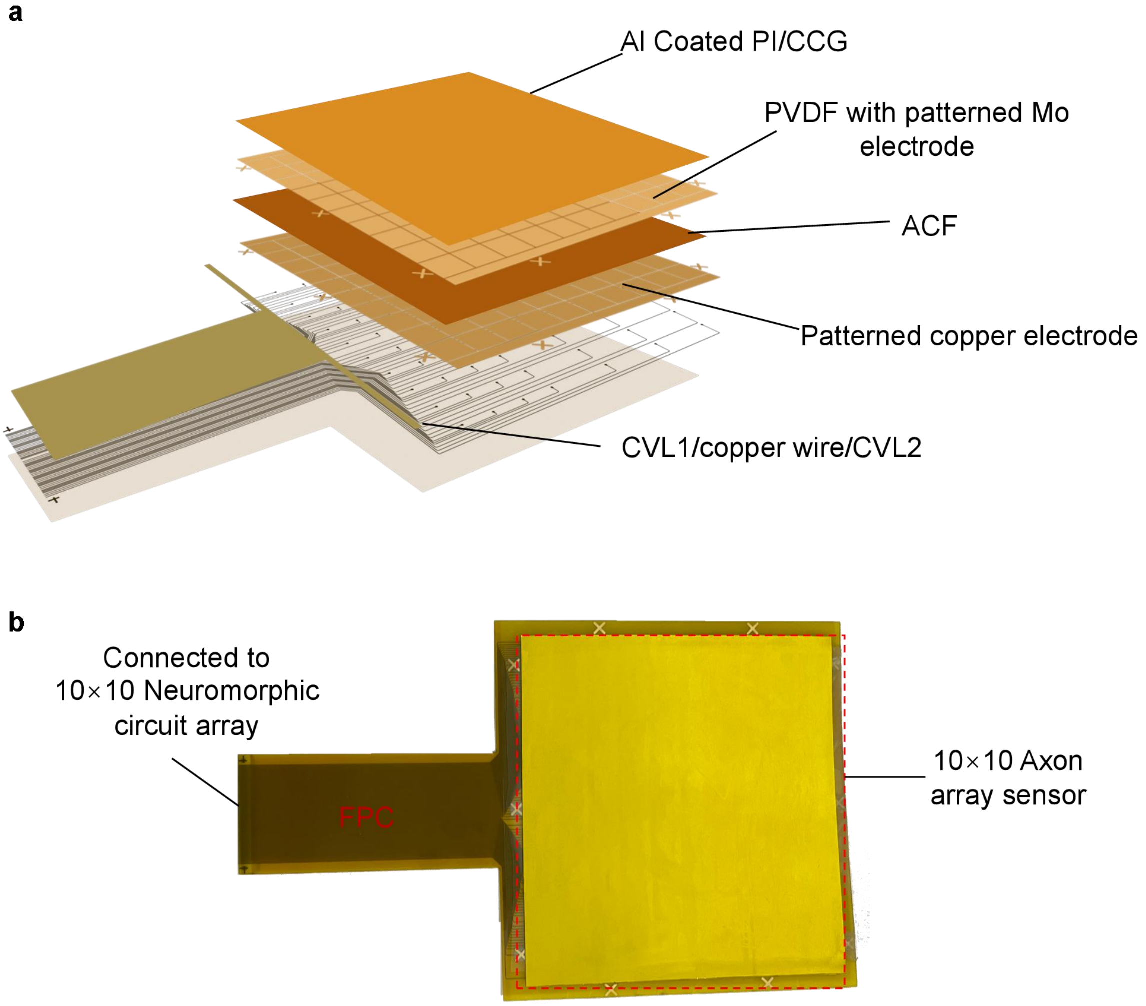

Supplementary Fig. 5. 10 × 10 artificial axon sensor. a, Schematic illustration. **b,** Photograph of a finished array (top) with an axon sensing unit size of 4.8 mm × 4.8 mm.

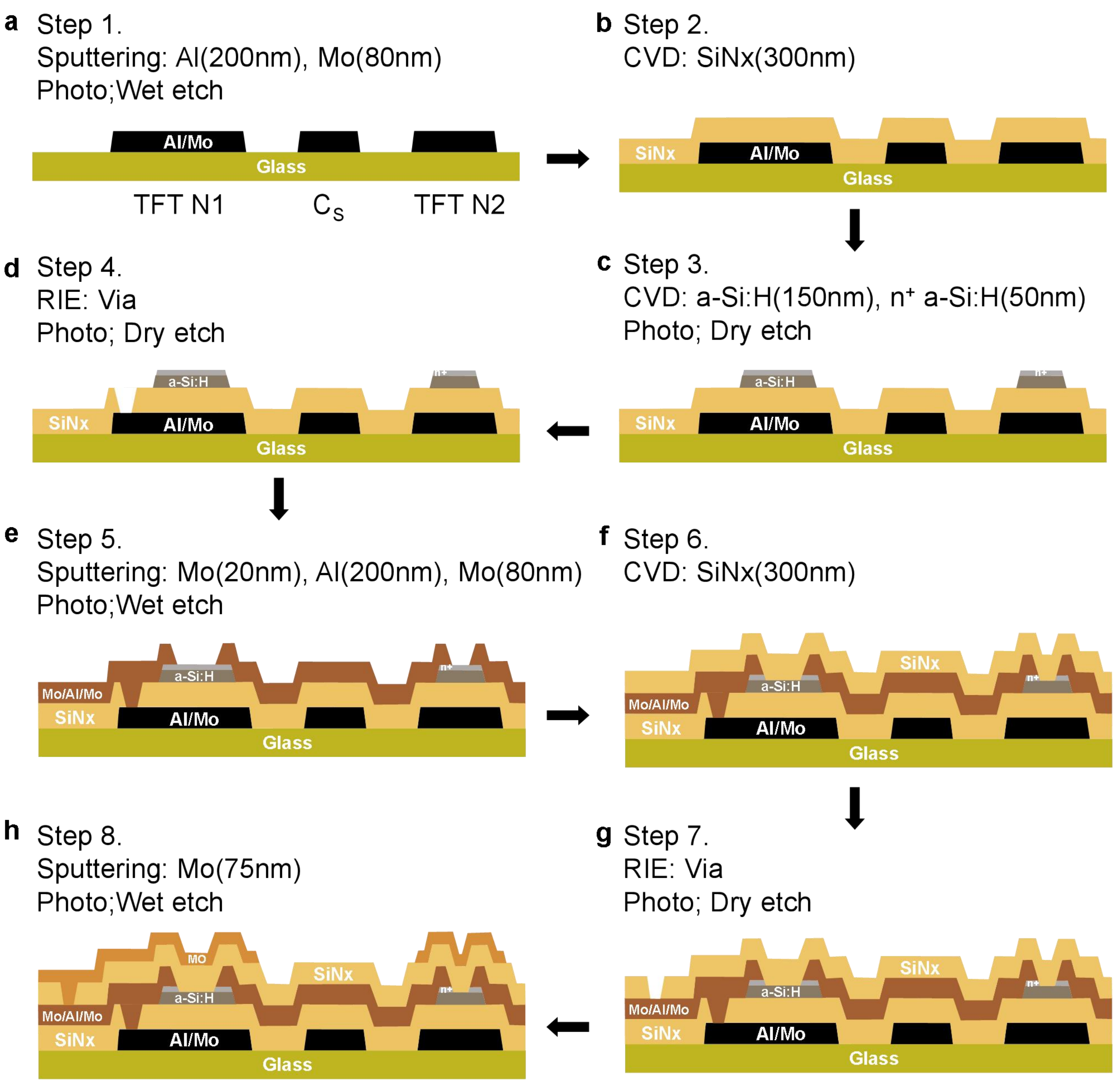

Supplementary Fig. 6. Schematic illustration of processing steps for fabricating 2T1C neuromorphic circuit. a, Aluminum (Al) and molybdenum (Mo) electrode were sputtered on the glass substrate and then patterned and wet etched. **b,** Silicon nitride (SiNx) material was deposited as dielectric layer. **c,** Hydrogenated amorphous silicon (a-Si:H) and n^+ a-Si:H were deposited and patterned. **d,** Via holes were etched by dry etching. **e,** Mo/Al/Mo layers were sequentially sputtered and patterned. **f,** SiNx layer was deposited. **g,** Via holes were created by dry etching. **h,** Mo electrode was sputtered and patterned.

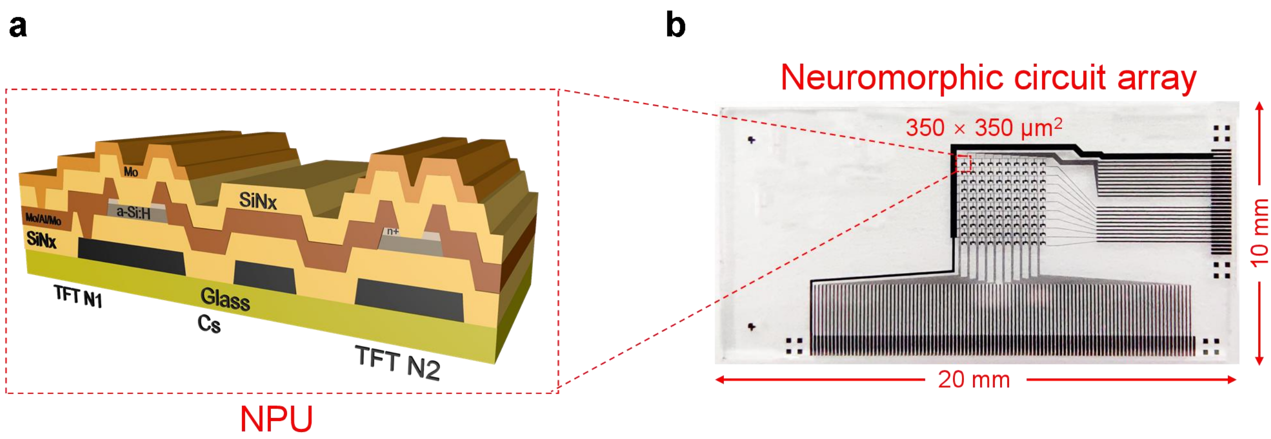

Supplementary Fig. 7. TFT-based neuromorphic circuit array. a, Schematic three-dimensional cross-sectional diagram of neural processing unit (NPU) with a size of 350 μm × 350 μm. **b,** Photograph of 10 × 10 neuromorphic circuit arrays on glass with a size of 20 mm × 10 mm.

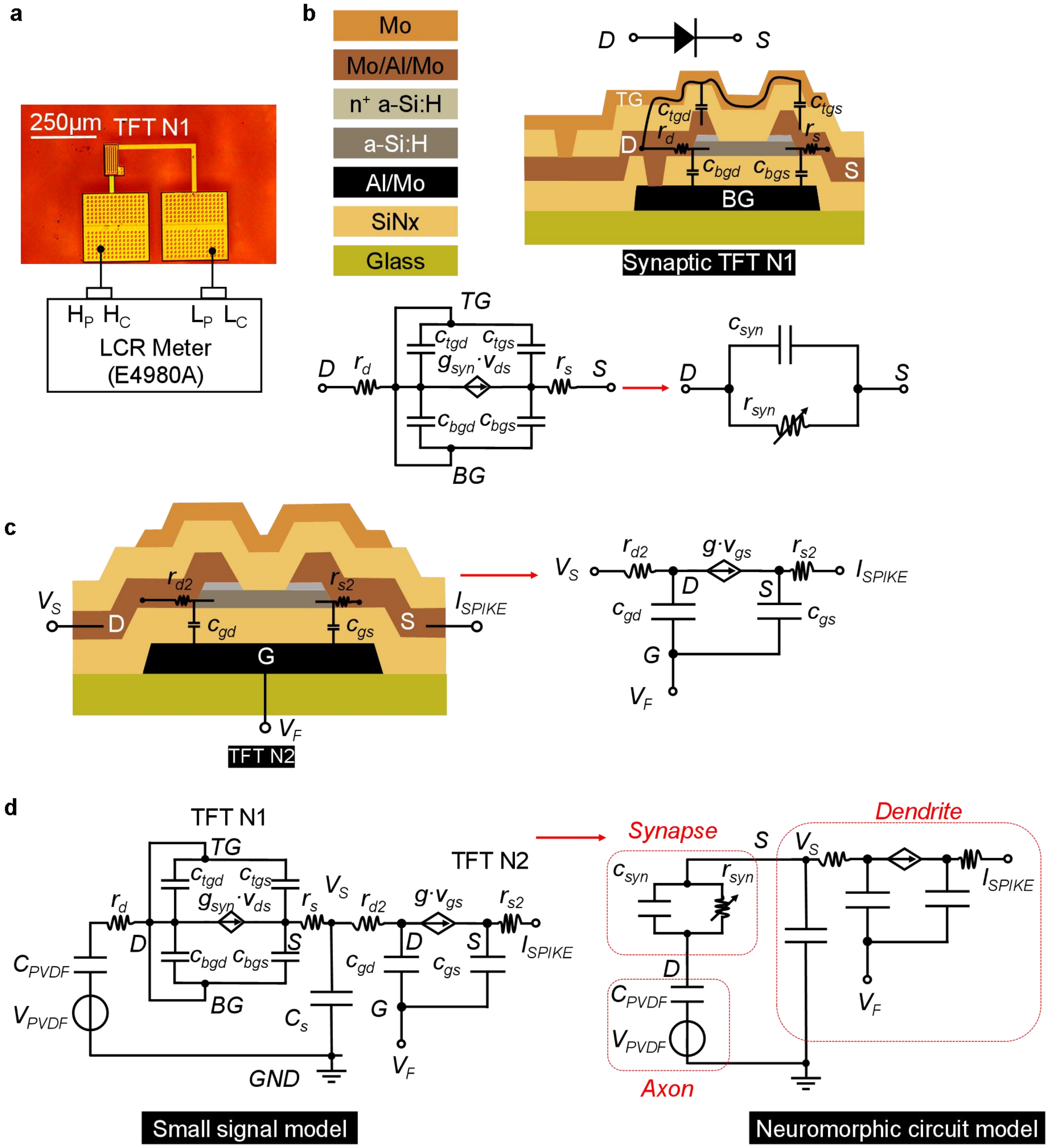

Supplementary Fig. 8. a, Microscopic photograph and LCR measurement of the synaptic TFT N1. **b,** Cross-sectional schematic view, small-signal equivalent circuit model and neuromorphic circuit model of TFT N1. Four gate-insulator capacitors of TFT N1 arise in parallel, namely, c_{tgd}, c_{bgd}, c_{tgs} and c_{bgs}. Due to the TG and BG of TFT N1 are shorted with the drain electrode, C_{tgd} and c_{bgd} are negligible. The contact resistance r_d and r_s are in series connection with voltage controlled current source ($g_{syn} \cdot v_{ds}$). The neurotransmitter release is imitated by the controlled source $g_{syn}{\cdot}v_{ds}$. **c,** Cross-sectional schematic view, small-signal equivalent circuit model of TFT N2. **d,** The small-signal equivalent circuit model and neuromorphic circuit model of NPU.

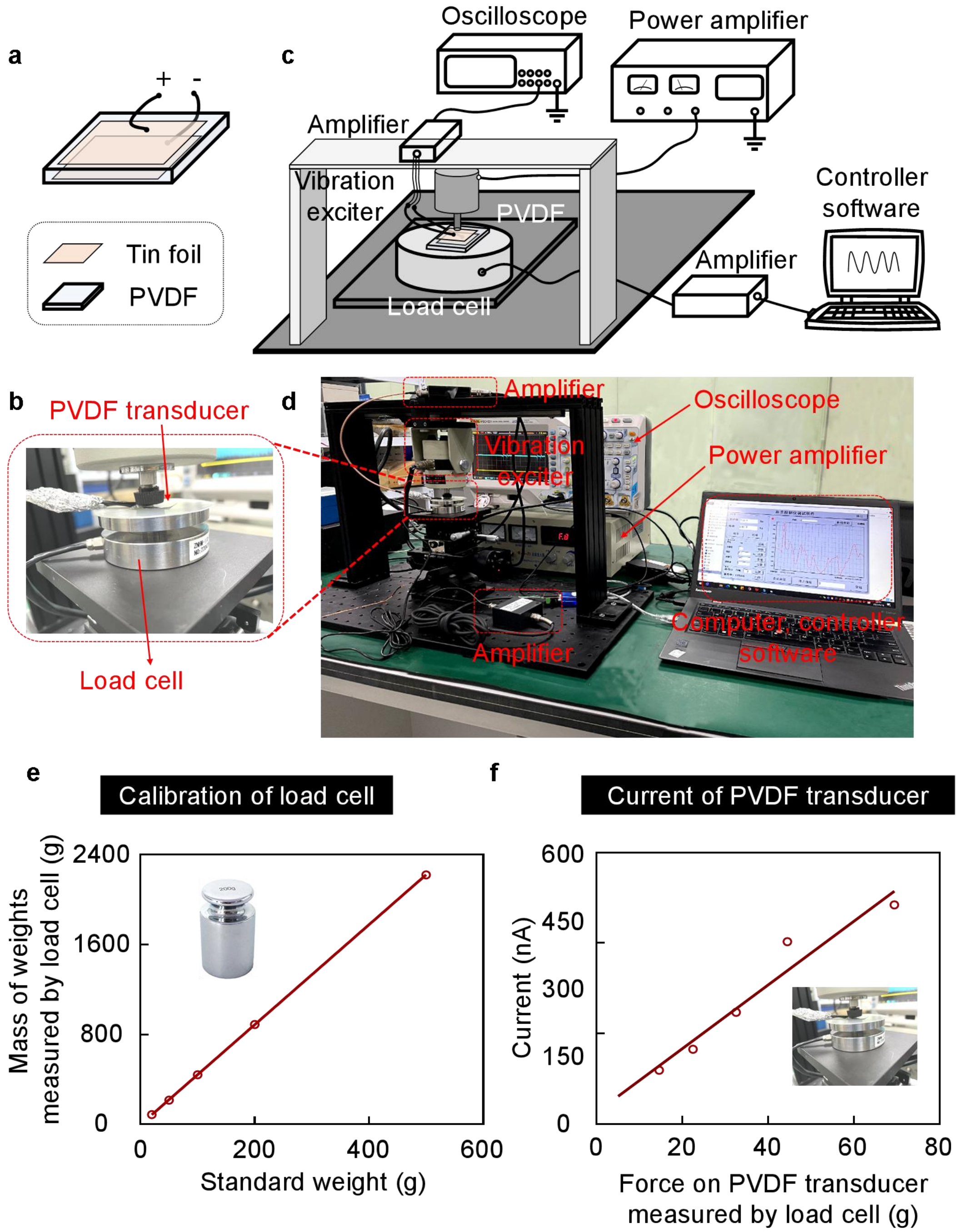

Supplementary Fig. 9. Experimental setup and initial evaluation of PVDF transducer (Supplementary Note 2). a, Sandwiched structure of PVDF transducer. **b,** The PVDF transducer and the load cell. **c,** Outline of the experimental setup. **d,** Experimental environment for investigating the generated current of PVDF transducer. **e,** Calibration of the load cell with standard weights. **f,** Relationship between the current measured by amplifier and the force on PVDF transducer obtained by load cell.

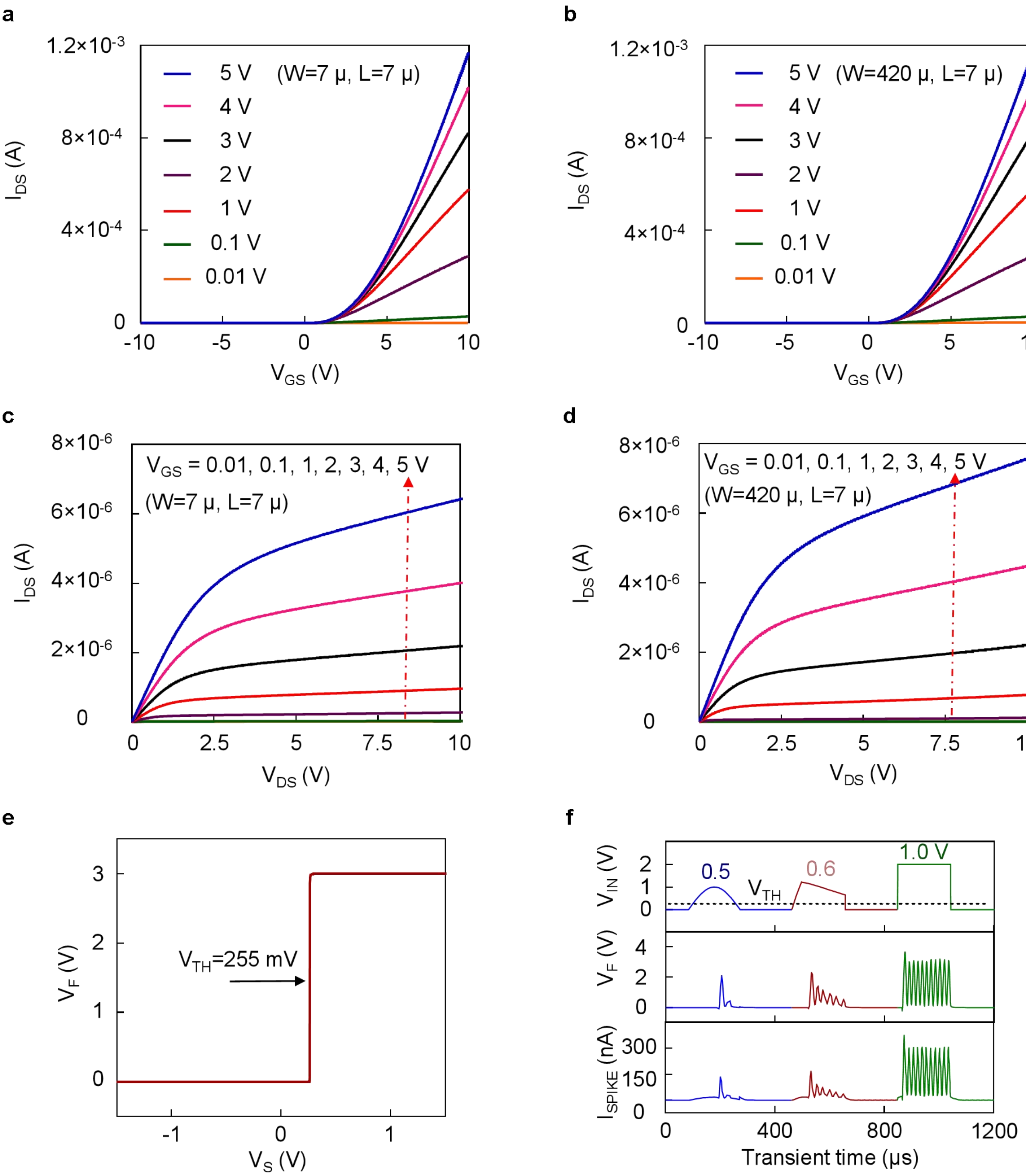

Supplementary Fig. 10. TFT-based neuromorphic process circuit simulation in Silvaco Tools. a, Transfer characteristics of the TFT with W/L = 7 μm/7 μm (V_{DS} = 0.01-, 0.1-, 1-, 2-, 3-, 4-, 5 V). **b,** Transfer characteristics of the TFT with W/L = 420 μm/7 μm (V_{DS} = 0.01-, 0.1-, 1-, 2-, 3-, 4-, 5 V). **c,** Output characteristics of the TFT with W/L = 7 μm/7 μm (V_{GS} = 0.01-, 0.1-, 1-, 2-, 3-, 4-, 5 V). **d,** Output characteristics of the TFT with

W/L = 420 μm/7 μm (V_{GS} = 0.01-, 0.1-, 1-, 2-, 3-, 4-, 5 V). **e,** Output voltage of the comparator circuit. **f**, When different types and strength of tactile inputs (sin:0.5, exp:0.6, and pulse:1.0 V, 192.5 μs duration time) were applied to the NPU, exhibiting faster firing time (36.3-, 14.9-, 0.3 μs) and higher the I_{SPIKE} occur. The NPU is capable of encoding different types of tactile inputs.

a

Parameter	Value
Vth	0.52 V
S-slope	0.4 V/dec
Ion/Ioff	1.4×10^4
μ	$0.3\ cm^2V^{-1}S^{-1}$

b

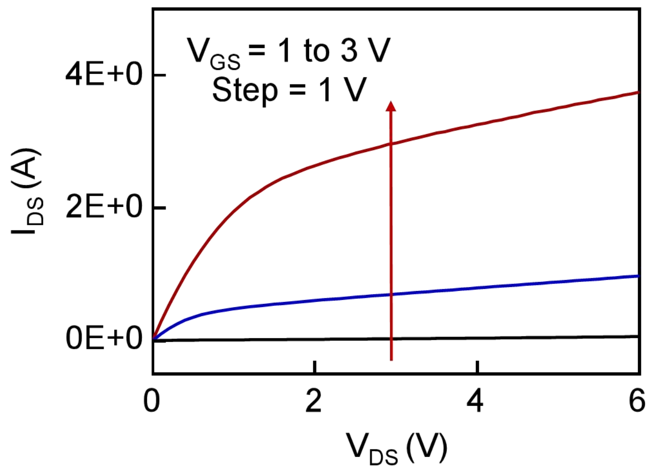

Supplementary Fig. 11. The firing switch of TFT N2. a, Fundamental device parameters extracted from the current-voltage curves. **b,** Output characteristics of the TFT N2.

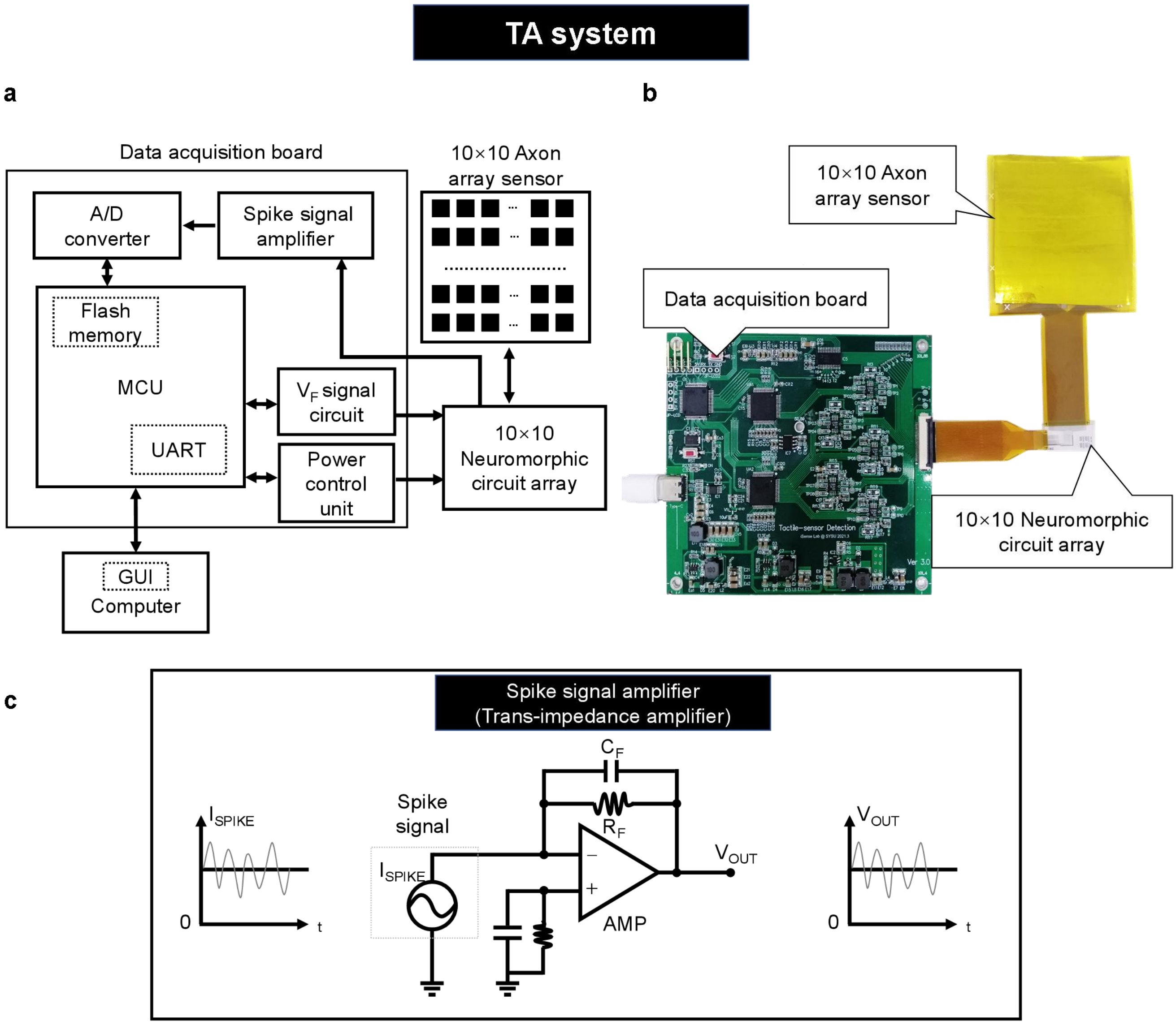

Supplementary Fig. 12. a, Design block diagram and architecture of the data acquisition system (DAB). **b,** Photograph of the DAB. **c,** Spike signal amplifier of the DAB is a trans-impedance amplifier, and the I_{SPIKE} current is converted into an output voltage (V_{OUT}).

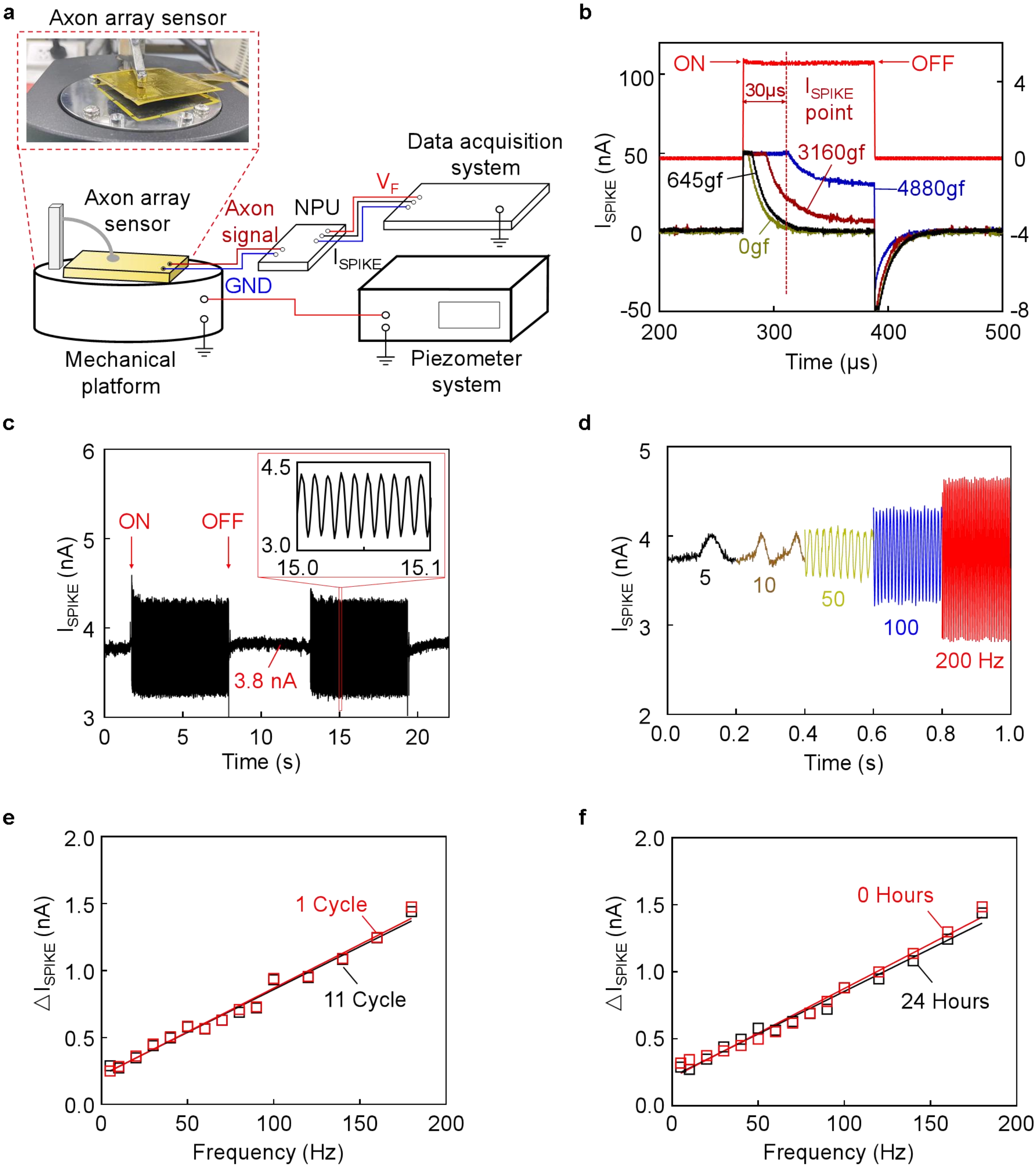

Supplementary Fig. 13. a, Schematic diagram of the experimental setup to evaluate performance of tactile scanner. **b**, I_{SPIKE} and V_F as a function of transient time with different tactile pressures (0-, 645-, 3160-, 4880 gf). The tactile scanner's acquisition rate is 1 kHz, the duration time of V_F is 110 μs. **c**, I_{SPIKE} as function of transient time during exposure to pressure generated by a mechanical platform. **d**, Vibration-sensing capability of the tactile scanner with vibration frequencies (5-, 10-, 50-, 100-, 200 Hz, 21.7 kPa). **e**, Variation of I_{SPIKE} of tactile scanner after 1 and 11 cycles of applied tactile inputs (21.7 kPa). **f**, Variation of I_{SPIKE} of tactile scanner after 0 and 24 hours of applied pressure (21.7 kPa).

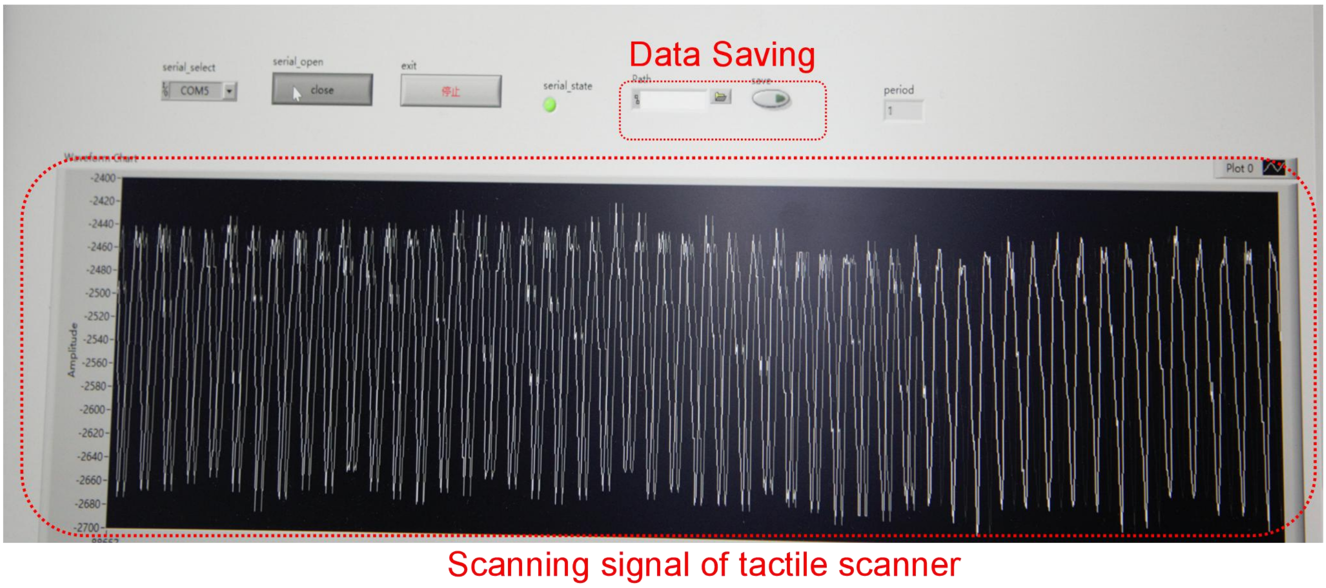

Supplementary Fig. 14. Graphical user interface (GUI), which is an in-house visualization software, has been developed particularly for the tactile scanner. The GUI can visualize the real-time collected waveforms of vibrotactile signal.

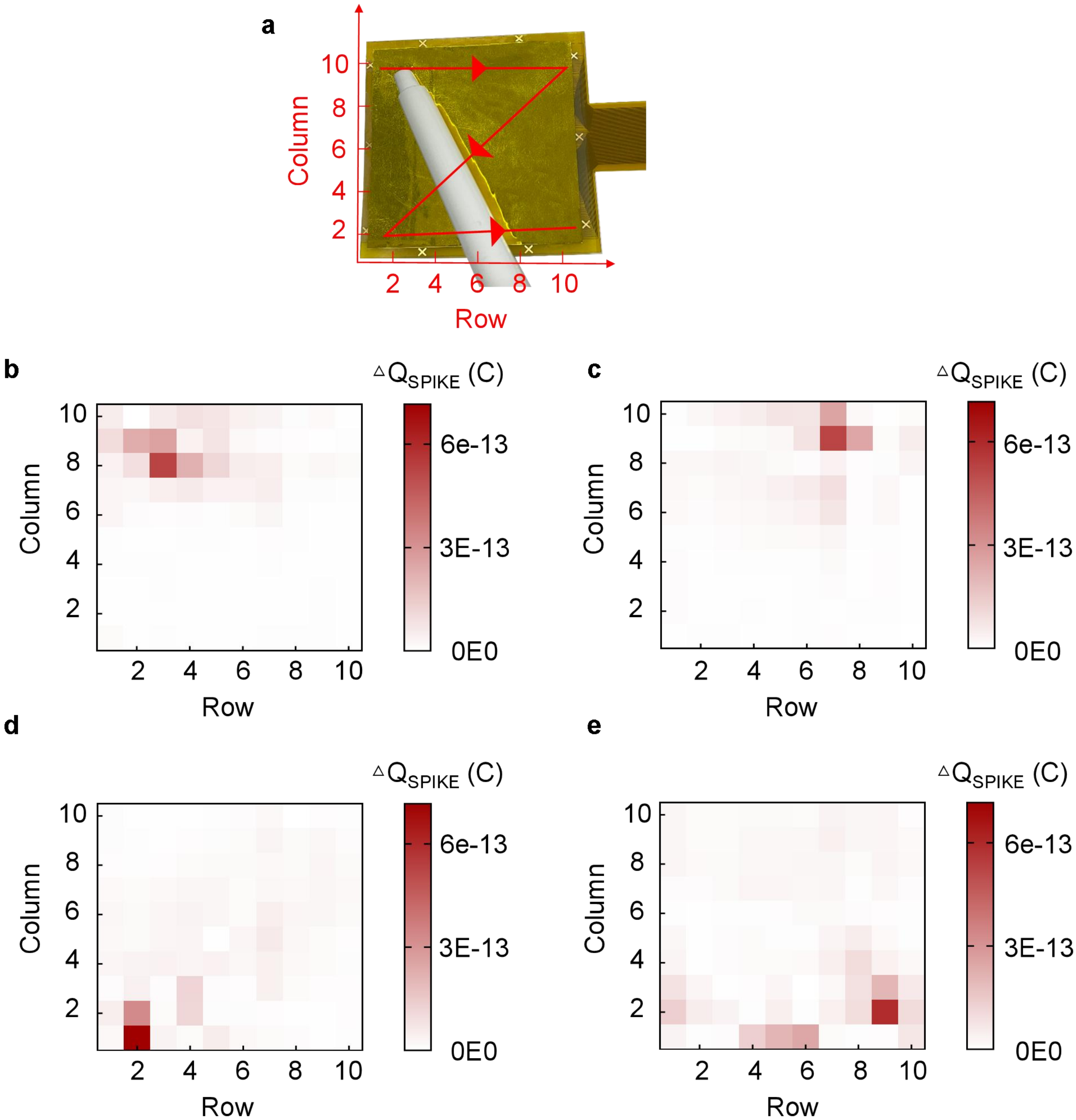

Supplementary Fig. 15. Test and visualization of a "Z" sliding event. a, Photographic description of the sliding event test. **b,** Visualized response of the array at a time interval of 0 second. **c**, 0.20 second. **d**, 0.80 second. **e**, 1.67 seconds.

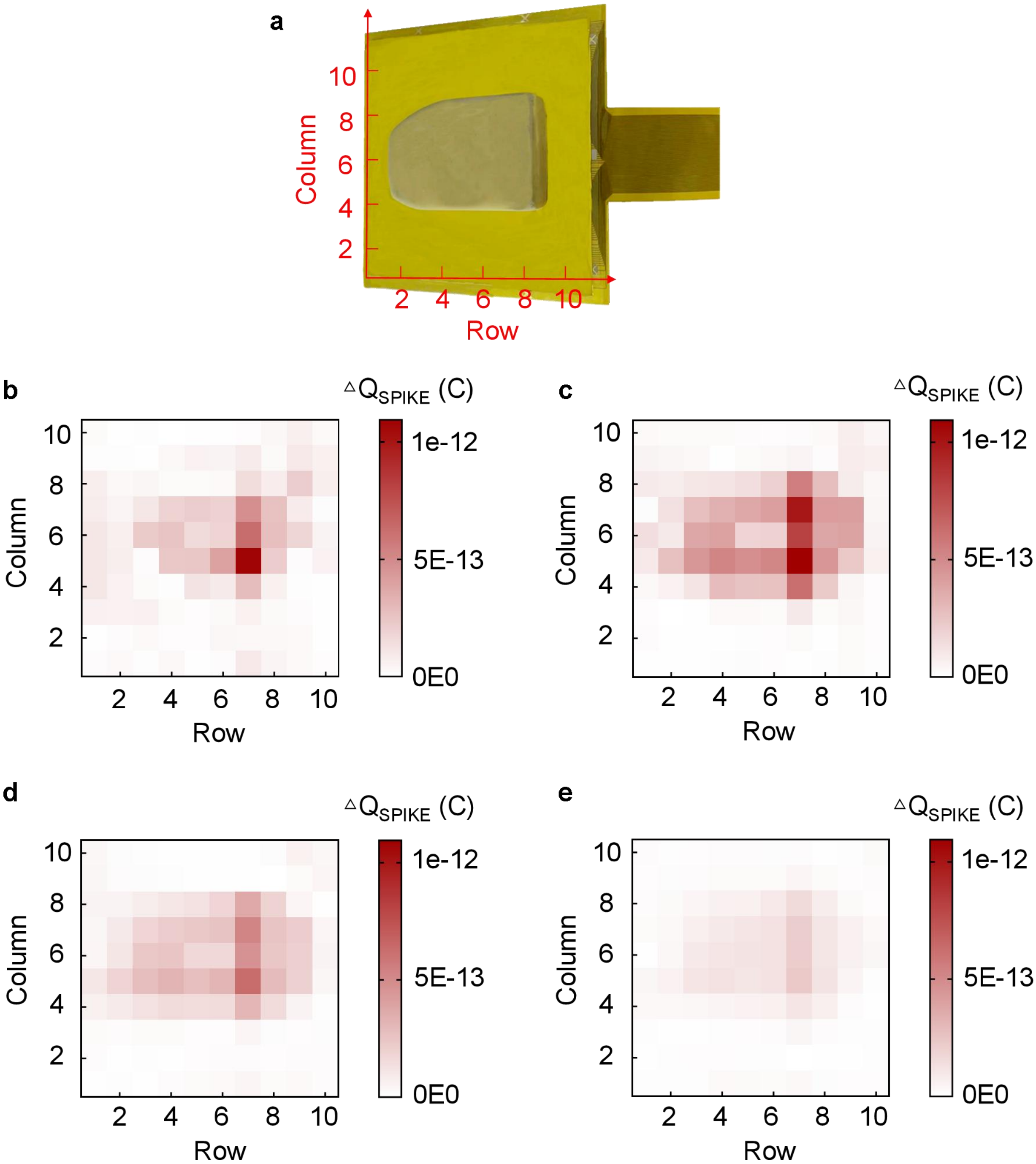

Supplementary Fig. 16. Test and visualization of "Eraser" weighting event. **a,** Photographic description of the weighting event. **b,** Visualized response of the array at a time interval of 0 second. **c,** 0.80 second. **d,** 1.17 seconds. **e,** 2.47 seconds.

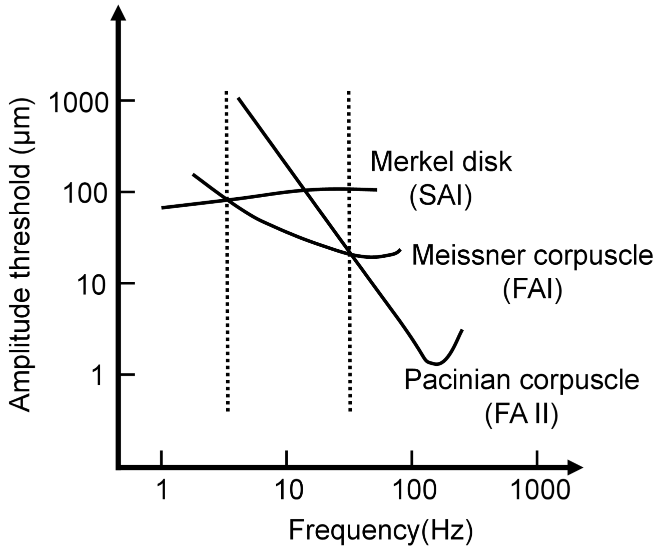

Supplementary Fig. 17. Amplitude threshold as a function of frequency for different mechanoreceptors. Several investigators have demonstrated that the SAI tends to be easily excited at low frequencies[15]. As the frequency improves, the slow adaptation becomes dominant, and the fast adaptation exhibits a decreasing trend[16-17]. The FAI is more associated with low-frequency vibrations (1-10 Hz)[18], while the FAII is more sensitive to the vibratory stimuli, at a frequency of above 200 Hz[19].

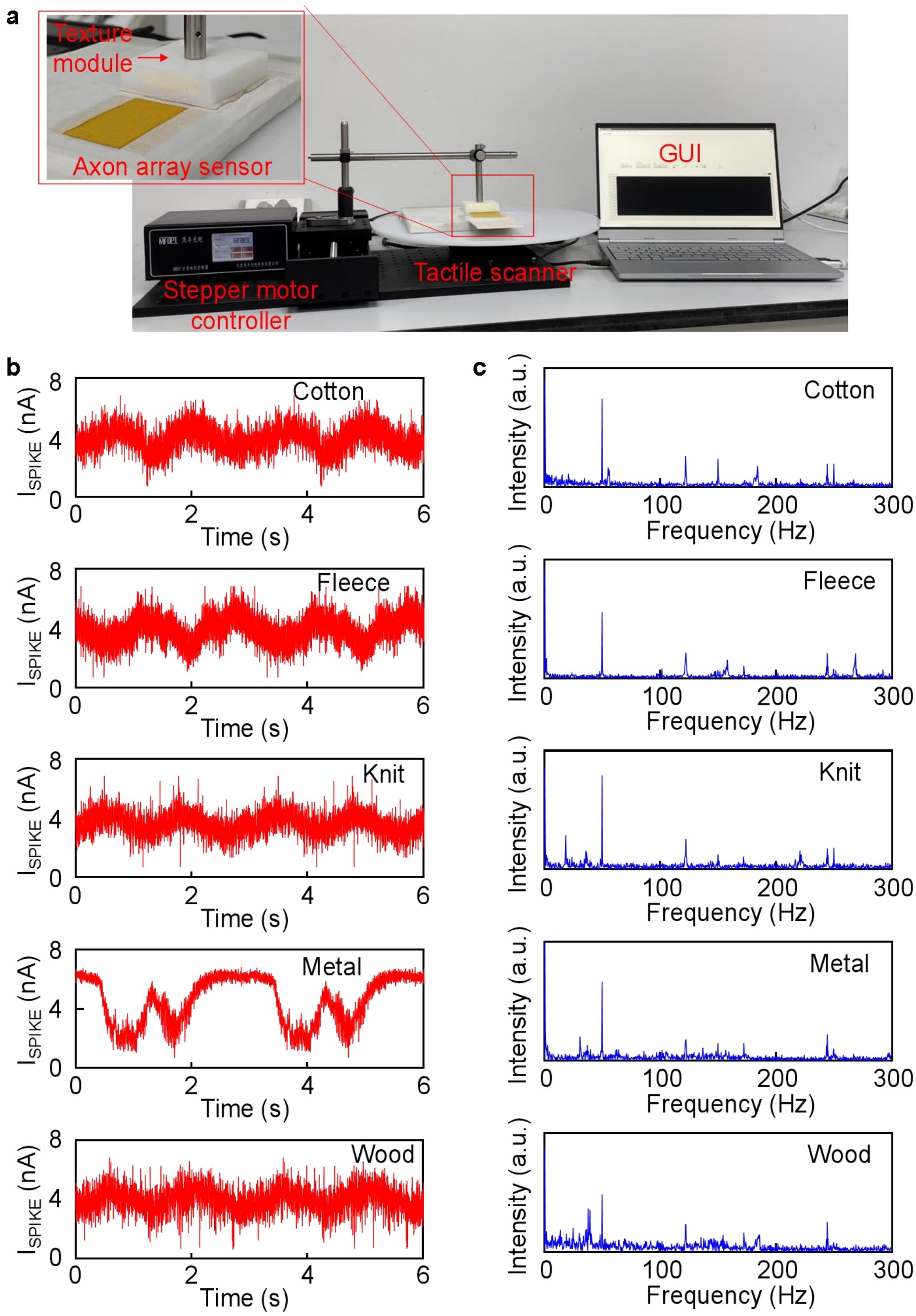

Supplementary Fig. 18. a, Images of the experimental set-up. The tactile scanner is connected to the GUI, and the test module housing the textured material is controlled by the stepper motor controller. **b,** The I_{SPIKE} of the NPU when sliding on different kinds of surface textures with a time interval of 6 seconds (cotton, fleece, knit, metal, and wood). **c,** Corresponding fast Fourier transform (FFT) results of I_{SPIKE} for five types of textures in **b**.

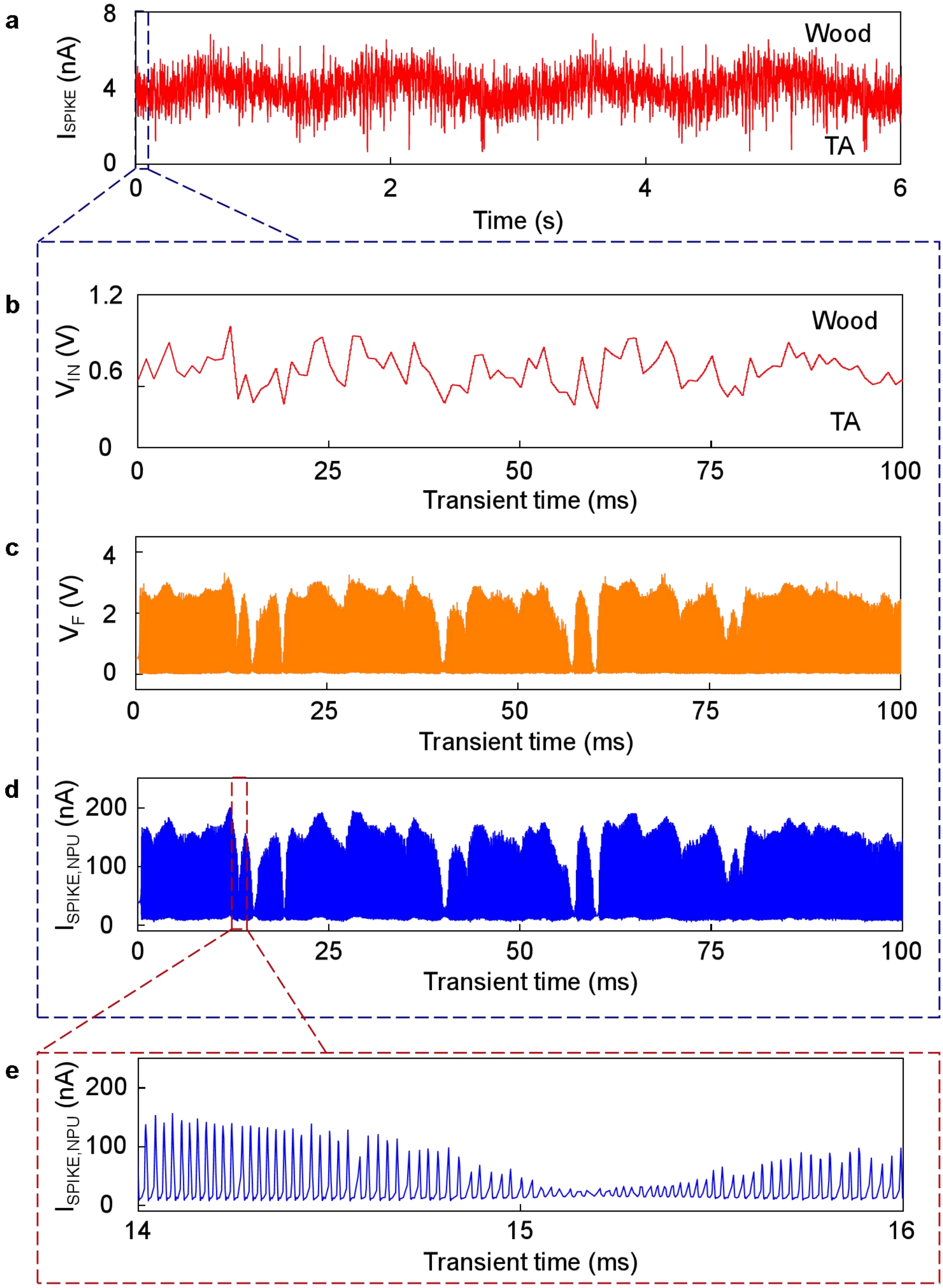

Supplementary Fig. 19. a, I_{SPIKE} (TA signals) when sliding on wood for 6 seconds. **b**, I_{SPIKE} converted to V_{IN} ($\leqslant$1 V) as inputs of the NPU circuit in Supplementary Fig.10 for simulation. **c**, V_F of the NPU circuit. **d**, I_{SPIKE} of the NPU circuit. **e,** Detailed I_{SPIKE} in **d** from 14- to 16 ms, demonstrating that NPU circuit is able to encode the tactile inputs.

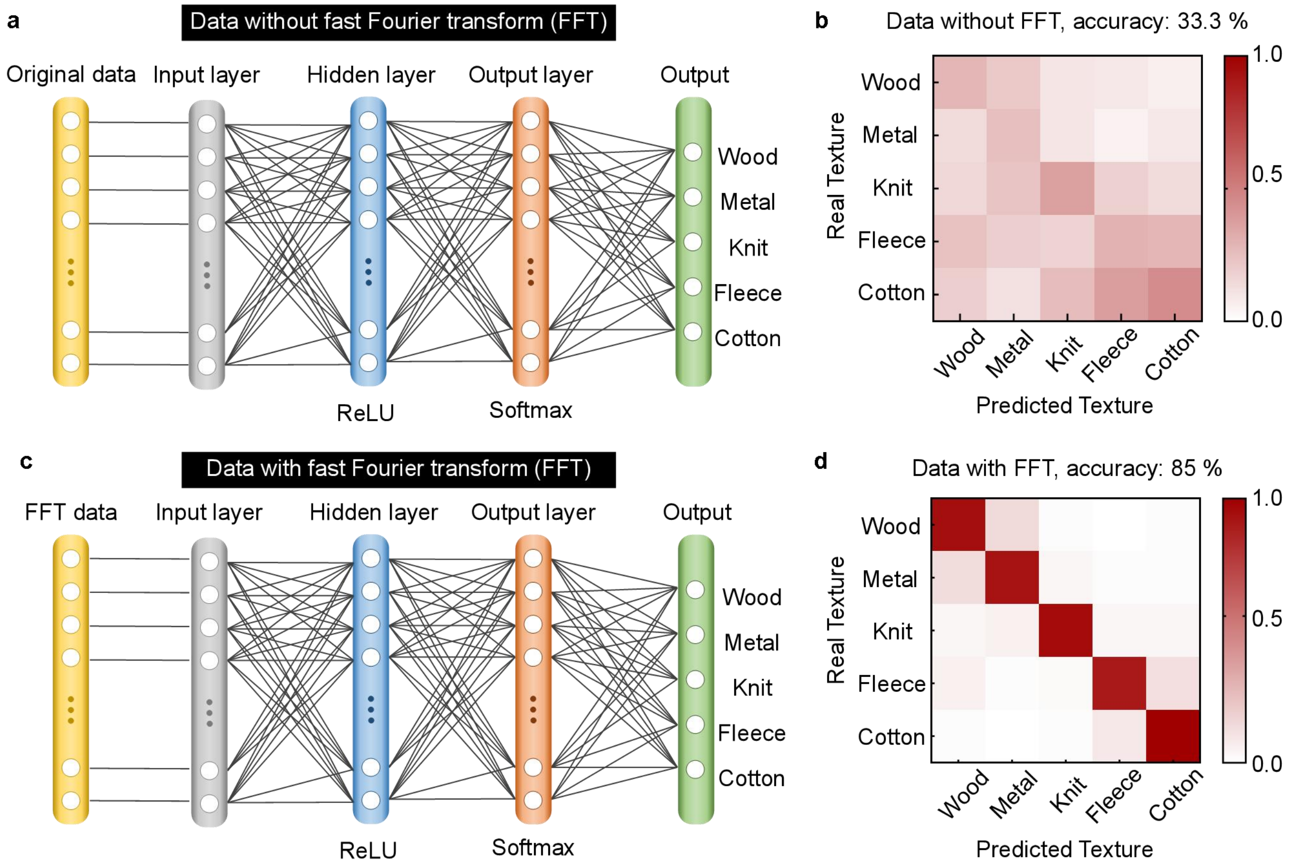

Supplementary Fig. 20. a, Artificial neural network (ANN) framework of the classification algorithm of tactile acquisition (TA) information of five textures (cotton, fleece, knit, metal, and wood) without fast Fourier transform (FFT). **b,** Results of classification matrix for textures without FFT processing in **a**, Classification accuracy is approximately 33.3%. **c,** ANN framework of classification algorithm of TA with FFT**. d,** Results of classification matrix for textures with FFT processing in **c**, Classification accuracy is approximately 85%.

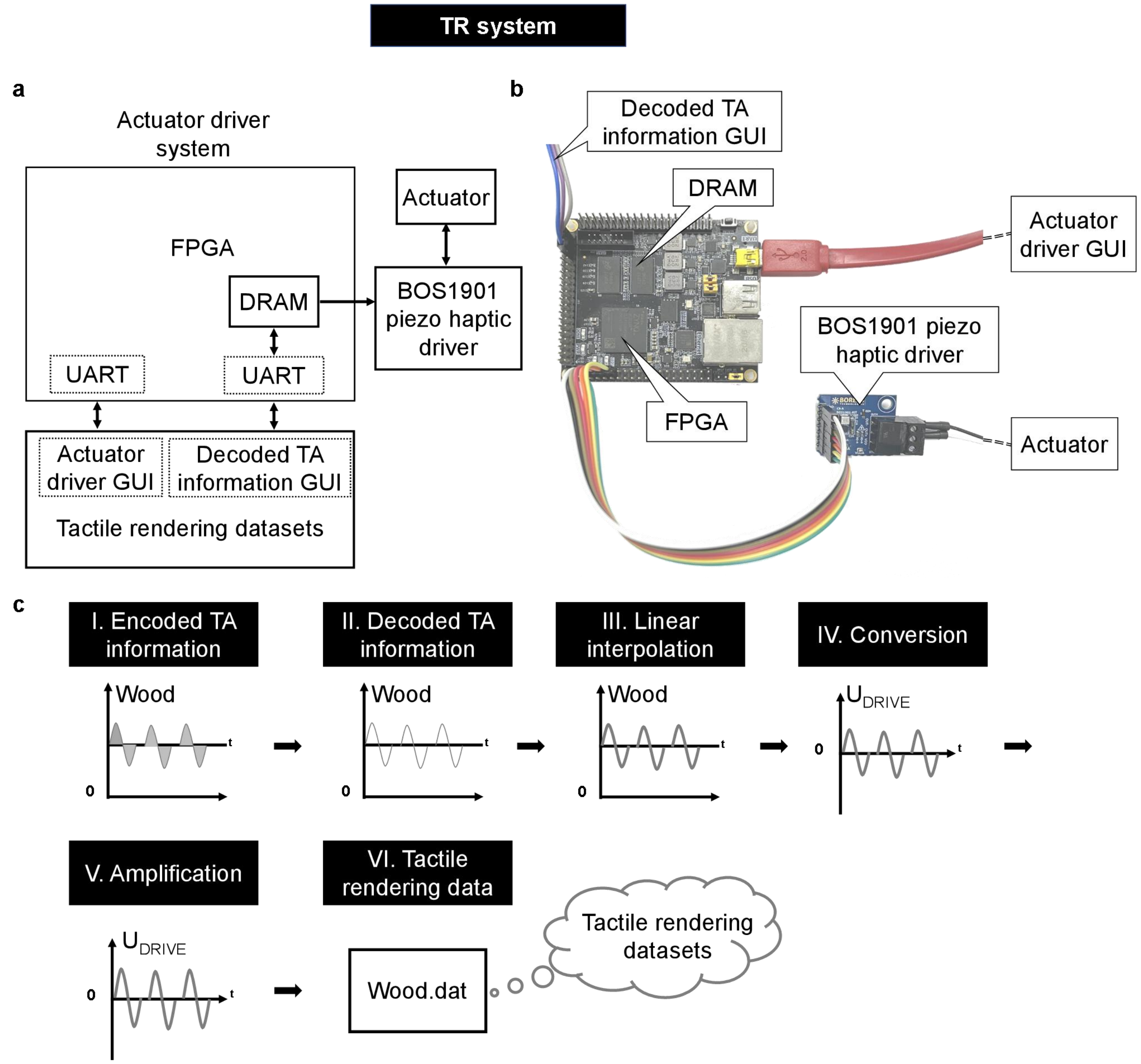

Supplementary Fig. 21. a, Design block diagram and architecture of actuator driver system with field programmable gate array (FPGA), dynamic random-access memory (DRAM), and two universal asynchronous receiver-transmitter (UART), and tactile rendering datasets (computer, controller software including actuator driver GUI, Tactile information GUI). **b,** Circuitry board of the haptic system. **c,** Illustration of the signal generation procedure of tactile rendering information in rendering datasets being used to drive the actuator.

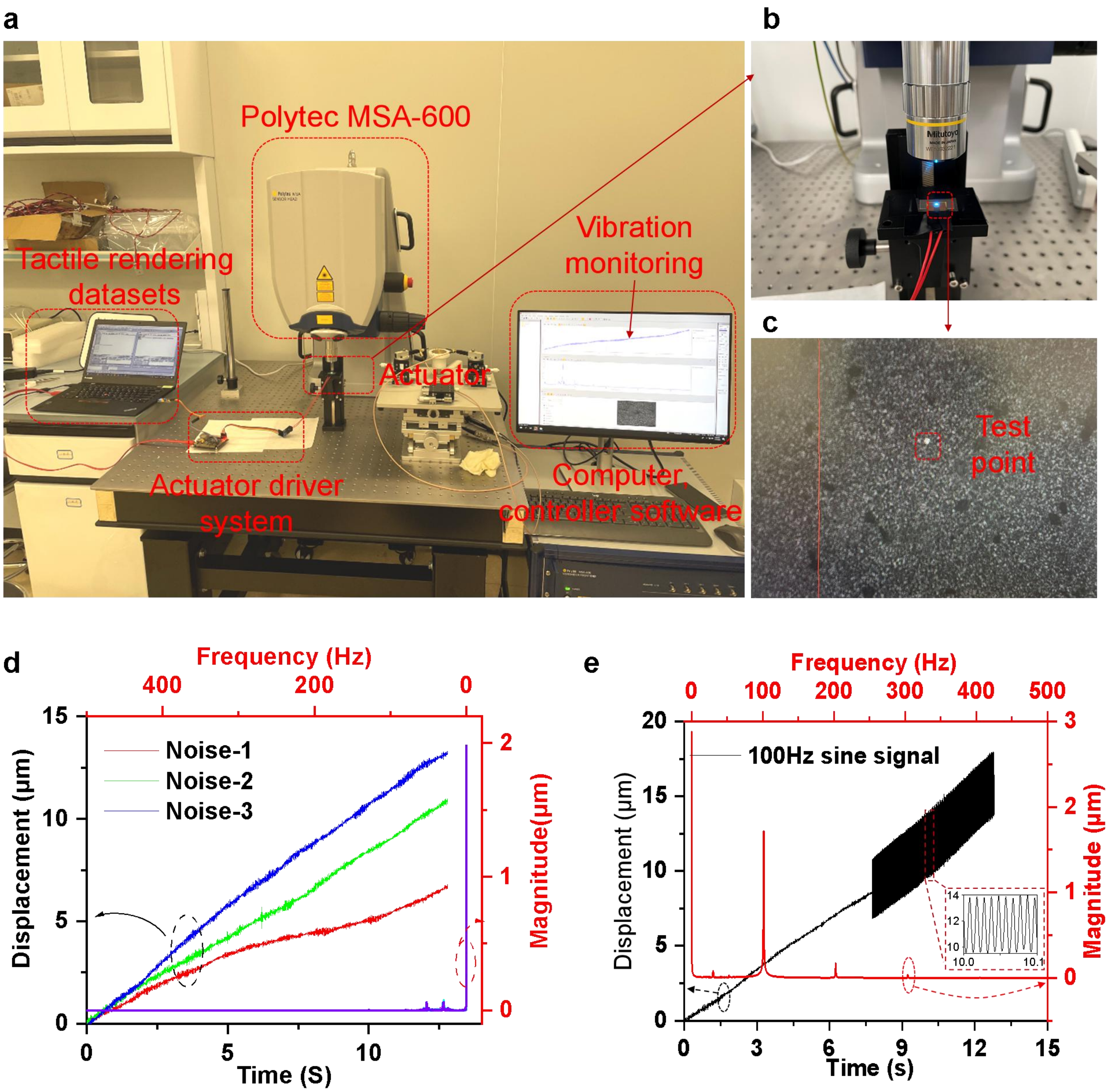

Supplementary Fig. 22. a, Experimental setup of capturing of tactile rendering signals at high resolution. **b,** Detail of the position of actuator. **c,** Microscopic image of the test point on the actuator. **d,** Displacement and frequency magnitude of vibration noise of Polytec MSA-600 Micro System Analyzer in ambient environment as a function of transient time and frequency. Three time periods of vibration noise were measured with 13 seconds (noise-1, noise-2, noise-3). The spectrum of right coordinate illustrates that the main vibration noise is mainly the drift noise(＜0.24 Hz). The other vibration noise is ± 0.18 μm, and the SNR ratio is 17 dB (Numerical analysis with tactile rendering (TR) signals of Fig.

6d). **e,** Transient time and frequency of sinusoid vibration signal with 100 Hz, indicating that the Polytec MSA-600 tester is capable of capturing vibration signal of actuator.

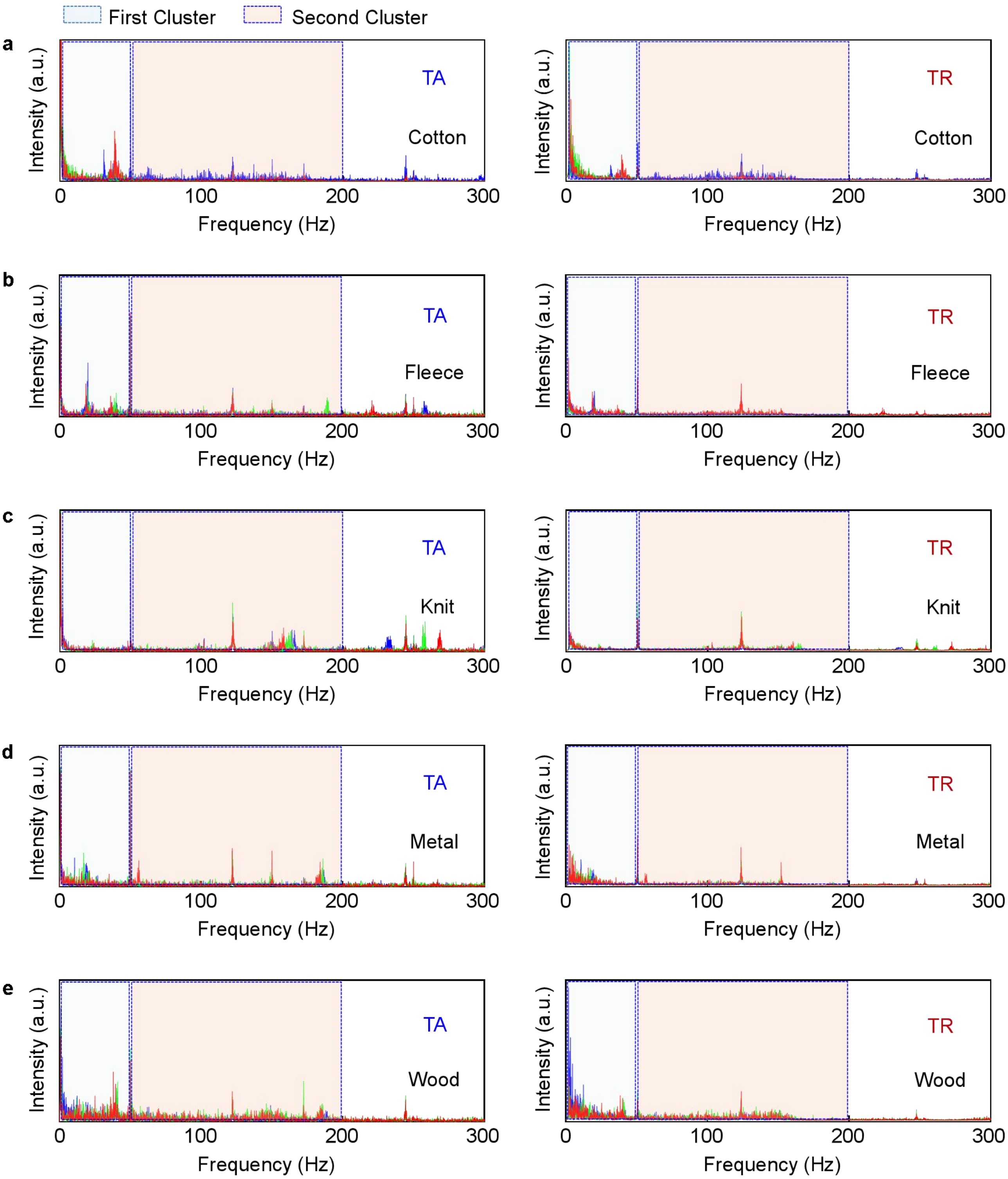

Supplementary Fig. 23. FFT amplitude-frequency characteristic curves of different textures between tactile acquisition signal (TA) and tactile rending signal (TR) with 6 seconds (three groups). a, Cotton. **b,** Fleece. **c,** Knit. **d,** Metal. **e**, Wood.

Supplementary Table 1 Characteristic comparison of reported tactile sensing system.

Mechanism	Material	Self-driven	Sensor interface	Functionality	Reference
Piezoresistive	Carbon nanotube	No	Synaptic device, Organic transistor	Sensorimotor loop[a], Sensory feedback[b]	Science 380, 6646 (2023)[1]
Piezoresistive	Carbon nanotubes, polyimide	No	Synaptic device, Organic transistor	Sensorimotor loop, Sensory feedback	npj flex. electron 6, 72 (2022)[2]
Piezoresistive	Carbon black /Ecoflex0030 composites	No	CMOS ICs	Somatosensory loop[c], Tactile rendering[d]	npj flex. electron 7, 1 (2023)[3]
Piezoresistive, piezoelectric	PDMS, PVDF-TrFE	No	CMOS ICs	Somatosensory loop, Tactile rendering	npj flex. electron 6, 82 (2023)[4]
Piezoelectric	**PVDF, polyimide**	**Yes**	**Synaptic device, Inorganic transistor, Neuromor-phic circuit**	**Somatosensory loop, Tactile rendering**	**This Work**

[a]Sensorimotor loop[1]: The sensorimotor loop is expected to emulate skin sensation and trigger feedback responses at the motor cortex.
[b]Sensory feedback[11-12]: The sensory feedback functions is bidirectional signal communication between perception and actuation, which elicits more intense reactions to stronger force stimuli.
[c]Somatosensory loop[3-4]: The characteristic of the somatosensory loop refers to perceive surface texture, shape, etc. And the surface information is conveyed to the human side by generating haptic feedback on the skin surface, enabling bilateral human-robot interactions.
[d]Tactile rendering[13]: The term is associated with the touch sensation of virtual products, such as intensity, roughness, texture, and other complex patterns, etc. It allows a human observer to feel the surface despite not touching the real object.

Supplementary Table 2 Process parameters of laminating axon sensor array.

	Instruction	Execution Unit	Status	Condition	Ref. Value
1.	Pump Opening	Pump Control			
2.	Wait Vacuum	Vacuum System		Lower than	50 mTorr
3.	Contact	Dynamic Control			
4.	Heating	Top-plate		Stop at	71℃
5.	Heating	Bottom-plate		Stop at	74℃
6.	Wait Temperature	Top-plate		Lower than	70℃
7.	Wait Temperature	Bottom-plate		Lower than	73℃
8.	Pressure	Dynamic Control		Set at	0.5 MPa
9.	Wait Time			Set at	10 min
10.	Pressure	Dynamic Control		Set at	0 MPa
11.	Heating	Top-plate			
12.	Heating	Bottom-plate			
13.	Wait Temperature	Top-plate		Lower than	100℃
14.	Wait Temperature	Bottom-plate		Lower than	100℃
15.	Contact	Dynamic Control			OFF
16.	Pump OFF	Pump Control		Set at	1.01 kPa
17.	Opening	Dynamic Control			

Supplementary Table 3 Device parameters of TFT-based neuromorphic circuit used in simulation.

Symbol	Parameter	Value	Unit
L	Length of TFT1/2/3/4/5/6	7	μm
W	Width of TFT1/4/6, TFT2/3/5	420,7	μm
$t_{channel}$	Thickness of semiconductor channel layer of TFT1/2/3/4/5/6	40	nm
$t_{dielectric}$	Thickness of dielectric layer of TFT1/2/3/4/5/6	160	nm
C_S	Capacitance	1.0	pF

Transfer characteristic and output characteristic, which were experimental testing (Supplementary Fig. 10), are extracted TFT models in Silvaco tools. The extracted models are used to preliminary verify the functions of NPU circuit.

Supplementary Note 1. Detail of biological model of sensory receptor and neuron, electron model of PVDF transducer and TFT-based neuromorphic circuit.

(i) Biological models of a neuron

Hodgkin-Huxley model

The Hodgkin-Huxley model (HHM) was proposed from the giant axon of the squid, suggesting that the electrical behaviour of the membrane may be represented by the network (Supplementary Fig.2b). The total membrane current comprises current into a capacitor and ionic current[5-6],

$$I = C_M \frac{dV}{dt} + I_{Na} + I_K + I_L \tag{1}$$

$$I = C_M \frac{dV}{dt} + g_{Na}(E - E_{Na}) + g_K(E - E_K) + \overline{g_L}(E - E_L) \tag{2}$$

Where I is the total membrane current, V is the displacement of the membrane potential from its resting value, C_M is the membrane capacitance per unit area, t is time. I_{Na}, I_K, and I_L are ionic current of sodium, potassium and other ions, respectively. E_{Na}, E_K and E_L are the equilibrium potentials for the sodium, potassium and other ions. The ionic permeability of the membrane could be satisfactorily expressed in terms of ionic conductance (g_{Na}, g_K, and g_L).

For the sake of reasonable accuracy and sufficiently simple for theoretical calculation of the action potential, the conductance is described by,

$$I = C_M \frac{dV}{dt} + \overline{g_{Na}} \cdot m^3 h(E - E_{Na}) + \overline{g_K} \cdot n^4 (E - E_K) + \overline{g_L}(E - E_L) \tag{3}$$

$$\frac{dm}{dt} = \alpha_m(1 - m) - \beta_m m \tag{4}$$

$$\frac{dh}{dt} = \alpha_h(1 - h) - \beta_h h \tag{5}$$

$$\frac{dn}{dt} = \alpha_n(1 - n) - \beta_n n \tag{6}$$

Where $\overline{g_{Na}}$, $\overline{g_K}$ and $\overline{g_L}$ are ionic conductance per cm^2. While n represents the proportion of the potassium at the inside of the membrane, m represents the activating molecules on the inside, h represents the outside inactivating molecules on the outside. These parameters are dimensionless variable varying between 0 and 1. α_m, β_m, α_h, β_h, α_n, and β_n are transfer rate constants in the two directions (inside and outside), which vary with membrane voltage. Importantly, α and β are steady-state values of activation and inactivation, expressed as membrane voltage functions using the Boltzmann equation. The aforementioned equations presented here describe the electrophysiological properties of neuron with relatively accuracy.

Leaky Integrate-and-Fire Model

The Leaky Integrate-and-Fire (LIF) model is simplified model[7-8], the cell membrane acts like a capacitor (C_{Mem}) in parallel with an ion channel resistor (R_{Ions}) in line with a membrane voltage ($V_{Mem}(t)$) (Fig. 3c and Supplementary Fig.2c). The total input current ($I_{IN}(t)$) in the circuit is conserved and split into two components:

$$I_{IN}(t) = I_{R_{Ions}}(t) + I_{C_{Mem}}(t) \tag{7}$$

$$I_{IN}(t) = \frac{V_{Mem}(t) - V_{Rest}}{R_{Ions}} + C_{Mem}\frac{dV_{Mem}(t)}{dt} \tag{3}$$

The model assumes that the ionic conductance ($g_{Ions} = 1/R_{Ions}$) is a constant, τ_{Mem} ($\tau_{Mem} = R_{Ions} \cdot C_{Mem}$) as the membrane time constant of the neuron. Thus, the membrane voltage can be described as a one-order linear differential equation:

$$\frac{dV_{Mem}(t)}{dt} \cdot \tau_{Mem} = -(V_{Mem}(t) - V_{Rest}) + R_{Ions} \cdot I_{IN}(t) \tag{9}$$

Hypothetically, the derivative function is in the similar expression as the original function ($dV_{Mem}(t)/dt \propto V_{Mem}(t)$), and the solution is an exponential function of a time constant (τ_{Mem}). When $t = 0$, the membrane voltage is $V_{Mem}(0) = V_0$, $I_{IN}(t) = 0$, the solution to the differential equation is:

$$V_{Mem}(t) = (R_{Ions} \cdot I_{IN}(t) + V_{Rest}) + [V_0 - (R_{Ions} \cdot I_{IN}(t) + V_{Rest})]\exp(-\frac{1}{R_{Ions}C_{Mem}} \cdot t) \tag{10}$$

During the resting period, the membrane potential remains a constant as a rest voltage (V_{Rest}). When the membrane potential rises to a constant threshold voltage (V_{thr}), a spike is triggered, and V_{Rest} then “resets” to a resting potential.

(ii) Biomimetic electrical models of PVDF transducer, TFT-based neuromorphic circuit

The piezoelectric transducer is based on piezoelectric effect that electrical charges are generated in certain types of solid materials when a force stimulus is applied. The piezoelectric-generated charges (Q_{PVDF}) of PVDF transducer are governed by the following equations written in the stress-charge format[9]:

$$Q_{PVDF} = d_{33} \cdot F_{33} + \frac{l}{t} d_{31} \cdot F_{31} \quad (11)$$

F is the applied force, l is the length and t is the thickness of PVDF transducer. The d_{31} and d_{33} is known as the transverse and longitudinal coefficient, respectively. Therefore, the polarization of PVDF transducer is proportional to the applied force.

Upon the applied force, the gate bias of the synaptic transistor TFT N1 will be a function of Q_{PVDF} and the equivalent capacitance of PVDF transducer (C_{PVDF}). Under such condition, the voltage generated by the PVDF transducer (V_{PVDF}) is also calculated by,

$$V_{PVDF} = V_{TG} = V_{BG} = \frac{Q_{PVDF}}{C_{PVDF}} = \frac{d_{33} \cdot F_{33} + \frac{l}{t} d_{31} \cdot F_{31}}{C_{PVDF}} \quad (12)$$

The r_{syn} is synaptic resistance, the r_d *is* drain resistance, the r_s is source contact resistance. The equivalent resistance (r_{eq}) of synaptic TFT is given by,

$$r_{eq} = r_{syn} + r_d + r_s \quad (13)$$

The gate-insulator capacitance is c_{syn} ($c_{syn} = c_{tg} + C_{bg}$). The c_{tg} (c_{tgd} is negligible, $c_{tg} = c_{tgs}$) and C_{bg} (c_{bgd} is negligible, $C_{bg} = c_{bgs}$) are the capacitance of the top and bottom gate capacitance of the TFT N1. The equivalent capacitance of the NPU is expressed as:

$$c_{eq} = C_S + \frac{c_{syn} \cdot C_{PVDF}}{c_{syn} + C_{PVDF}} \quad (14)$$

Thus, the time constant (t) of the NPU is given as $\tau = r_{eq} \cdot c_{eq}$.

Since the tactile stimulus input for vibrotactile is generally weak, the gate bias voltage is lower than the threshold voltage but greater than zero. Hence, the synaptic TFT N1 works in the sub-threshold regime and the output current I_{DS} is given as below:

$$I_{DS} = I_{D0} \exp\left(\frac{q[(1+\gamma)V_{PVDF} - V_{TH1}]}{\beta \cdot kT}\right) \times \left[1 - \exp\left(\frac{-q \cdot (V_{PVDF} - V_S)}{kT}\right)\right] \quad (15)$$

Where I_{D0} is the output current when $V_{BG}=V_{TH1}$ and $(V_{PVDF}-V_S)<<-kT/q$. Here, V_{TH1} is the threshold voltage of TFT N1, q is the electron charge, k is the Boltzmann's constant, T is the absolute temperature in Kelvin, S is the sub-threshold swing, and β is related to S,

$\beta = q \cdot S / [(\ln 10) \cdot kT]$. When the tactile input is applied, the generated voltages (V_{PVDF}-V_S) is less than millivolts, thus the $[1 - \exp \frac{-q(V_{PVDF} - V_S)}{kT}]$ term is approximately equal to unity.

When t = 0, the tactile input is applied, the piezoelectric-generated charges $Q_{PVDF}(t)$ is a constant. The current of the storage capacitor (C_S) of NPU can be obtained:

$$\frac{dV_S(t)}{dt} \cdot C_S = I_{DS} \tag{16}$$

$$\frac{dV_S(t)}{dt} = \frac{I_{D0}}{C_S} \exp\left(\frac{q[(1+\gamma)(\frac{Q_{PVDF}(t)}{C_{PVDF}}) - V_{TH1}]}{\beta \cdot kT}\right) \tag{17}$$

Based on Eq. (17), the voltage of C_S can be further simplified as:

$$V_S(t) = V_0 + \frac{I_{D0}}{C_S} \exp\left(\frac{q[(1+\gamma)(\frac{Q_{PVDF}(t)}{C_{PVDF}}) - V_{TH1}]}{\beta \cdot kT}\right) \cdot t \tag{18}$$

Where the C_S initial voltage is V_0, and t is closely related to the time constant τ ($\tau = r_{eq} \cdot c_{eq}$).

Hence, as seen from theoretical analysis, the tactile signal acquisition of NPU is related to the design of the synaptic TFT N1, the firing switch TFT N2 and the storage capacitor C_S. The TFT-based NPU needs a compromise design to acquire tactile information.

Supplementary Note 2. Measurement of PVDF transducer

The PVDF transducer test unit were prepared on tin foil with a sandwiched structure. The thickness of PVDF film is 110 μm, and the area is 10×10 mm^2. Two out-leads were soldered on tailored tin foils, and the tin foils were conglutinated onto the surfaces of PVDF films by the conductive resin on the tin foils (Supplementary Fig.9a). The vibration motor was used to ensure the impacting force applied exactly on the PVDF transducer (Supplementary Fig.9b). The experimental setup and detection system were depicted in Supplementary Figs.9c and 9d, respectively.

Calibration was performed on the load cell and the mass for a given set of standard weights was measured. Here, five standard weights of 20-, 50-, 100-, 200-, and 500 g, were measured. The signal from the load cell was amplified by an amplifier (ZHBSQ-S-485), collected by an upper computer through a USB port, and analyzed by a specific software developed by SENSING DATA DISPLAY SYSTEM from BENGBU CHINO SENSOR Co., Ltd. Supplementary Fig.9e is a typical plot from the load cell calibration, demonstrating that the result exhibits approximately a linear function.

The piezoelectric-generated charges (Q_{PVDF}) generated by the PVDF transducer were introduced into the IV-AMP 1616L trans-impedance amplifier (1 MV/A gain coefficient, 1 MHz bandwidth, KANG WEI TECHNOLOGIES Co. Ltd.), the charge variation could be transformed to voltage signal, and voltage signal was saved by MSO4024 oscilloscope (RIGOL TECHNOLOGIES Co. Ltd.). The op amp's output voltage (V_{OUT}) is:

$$V_{OUT} = -I_{PVDF} \cdot R_F \tag{19}$$

The feedback resistance (R_F) is 1 MΩ, the numerical current response I_{PVDF} ($I_{PVDF} = dQ_{PVDF}/dt$) are presented in Supplementary Fig.9f and Fig. 4b.

Supplementary Note 3. Acquisition of tactile rendering signal at high resolution

To characterize the tactile rendering signals of different textures recreated by the actuator, a force sensor-integrated equipment is used to acquire the rendered tactile signals for comparison. Here, we use a high-resolution MEMS dynamic analyzer, Polytec MSA-600 Micro System Analyzer (Supplementary Fig.22a). The vibration of the actuator is analyzed by using laser Doppler method under a standard atmospheric pressure with 532-nm laser. The actuator was fixed on an anti-vibration table to guarantee the laser pointing exactly on the test point of actuator (Supplementary Fig.22b).

The vibration-induced noise under atmospheric testing environment is low. As shown in Supplementary Fig.22d, the vibration-induced noise (Noise-1, Noise-2, Noise-3) changes over time. According to spectrum analysis, there is a negligible noise signal below 0.24 Hz. To confirm that the actuator produces tactile stimulus signal similar to that of the texture, a 100 Hz sinusoidal vibration is generated by the actuator (PHUA3015-30A-21-000, TDK Co. Ltd.), and the vibration signal of the actuator was measured by the Polytec MSA-600 Micro System Analyzer. As shown in Supplementary Fig.22e, a 100 Hz sinusoidal vibration signal can be identified.

According to the spectrum of five-type textures (Supplementary Fig.23), the feature information obtained by the tactile scanner are clustered at the low frequency (< 200 Hz). And because the actuator can effectively detect a 100-Hz sinusoidal signal, it should not be problematic to capture the spatiotemporal features of the textures.

Supplementary Note 4. Spearman's correlation coefficient of TA and TR signals

In order to check the similarity between TA signals collected by tactile scanners and TR signals obtained by MEMS dynamic analyzer, the spearman's correlation coefficient is attained and is also used to verify the tactile re-creation. The spearman's correlation coefficient (r) is given as:

$$r = \frac{\frac{1}{n}\sum_{i=1}^{n}(r(ta) - r(\bar{ta}))\cdot(r(tr) - r(\bar{tr}))}{\sqrt{(\frac{1}{n}\sum_{i=1}^{n}(r(ta) - r(\bar{ta}))^2)\cdot(\frac{1}{n}\sum_{i=1}^{n}(r(tr) - r(\bar{tr}))^2)}} \tag{20}$$

Where $r(ta)$ and $r(tr)$ are the ranks of the TA and TR signal variables, $r(\bar{ta})$ and $r(\bar{tr})$ are the mean ranks, n is the number of TA or TR data.

References in supplementary

S1. Wang, W. et al. Neuromorphic sensorimotor loop embodied by monolithically integrated, low-voltage, soft e-skin. *Science* **380**, 735-742 (2023).

S2. Sun, F. et al. An artificial neuromorphic somatosensory system with spatio-temporal tactile perception and feedback functions. *npj Flex. Electron.* **6**, 72 (2022).

S3. Chen, S. et al. Skin-integrated stretchable actuators toward skin-compatible haptic feedback and closed-loop human-machine interactions. *npj Flex. Electron.* **7**, 1 (2023).

S4. Jin, H. et al. Highly pixelated, untethered tactile interfaces for an ultra-flexible on-skin telehaptic system. *npj Flex. Electron.* **6**, 82 (2022).

S5. Hodgkin, Alan L. et al. A quantitative description of membrane current and its application to conduction and excitation in nerve. *J. physiol.* **117**, 500-544 (1952).

S6. Börgers C. Three Simple Models of Neurons in Rodent Brains. In: An Introduction to Modeling Neuronal Dynamics. *Texts in Applied Mathematics.* **66**, 31-37 (2017).

S7. Thorpe, S. J. Spike arrival times: A highly efficient coding scheme for neural networks, *Parallel processing in neural systems and computers*, 91-94(1990).

S8. Thrope, B. et al. Rank order coding, *Computational Neuroscience*, 113-118 (1998).

S9. Li, W. et al. A Force and Temperature Sensor Array Based on 3-D Field-Coupled Thin-Film Transistors for Tactile Intelligence. *IEEE Trans. Electron Devices.* **67**, 2890-2895 (2020).

S10. *Piezo Film Sensors Technical Manual*, (Measurement Specialties Inc. 2006).

S11. Chortos, A. et al. Pursuing prosthetic electronic skin. *Nat. Mater.* **15**, 937-950 (2016).

S12. Song, K. I. et al. Adaptive self-healing electronic epineurium for chronic bidirectional neural interfaces. *Nat. Commun.* **11**, 4195 (2020).

S13. Lin, W. et al. Super-resolution wearable electrotactile rendering system. *Sci. Adv.* **36**, eabp8738 (2022).

S14. Sakariya, K. et al. Leakage and charge injection optimization in a-Si AMOLED displays. *J. Display Technol.* **2**, 254-257 (2006).

S15. Abraira, V. E. et al. The Sensory Neurons of Touch. *Neuron.* **19**, 618-639 (2013).

S16. Verrillo, R. T. Effect of Contactor Area on the Vibrotactile Threshold. *J. Acoust. Soc.*

Am. **35**, 1962-1966 (1963).

S17.Johansson, R. S. et al. Responses of Mechanoreceptive Afferent Units in the Glabrous Skin of the Human Hand to Sinusoidal Skin Displacements. *Brain Res.* **244**, 17-25 (1982).

S18.Knibestol, M. Stimulus-response functions of rapidly adapting mechanoreceptors in human glabrous skin area. *J. Physiol.* **232**, 427-452 (1973).

S19.Hunt, C. C. On the Nature of Vibration Receptors in the Hind Limb of the Cat, *J. Physiol.* **155**, 175-186 (1961).